Tumor-Homing, Size-Tunable Clustered Nanoparticles for Anticancer Therapeutics

Jinhwan Kim,[†,‡] Yeong Mi Lee,[†,‡] Youngnam Kang,[†,‡] and Won Jong Kim[*,†,‡]

[†]Center for Self-assembly and Complexity, Institute for Basic Science (IBS), Pohang 790-784, Korea, and [‡]Department of Chemistry Polymer Research Institute, Pohang University of Science and Technology (POSTECH), Pohang 790-784, Korea

ABSTRACT We present herein a pH-responsive dynamic DNA nanocluster based on gold nanoparticles with highly packed nucleic acid assembly and evaluate its potential as a drug delivery vehicle with tumor-specific accumulation. Each gold nanoparticle was readily functionalized with various functional DNA sequences; in particular, we modified the surface of gold nanoparticles with bcl-2 antisense and i-motif binding sequences. Clustering of the gold nanoparticles induced by hybridization of each DNA sequence *via* i-motif DNA provided tumor targeting and drug loading capabilities. After cellular uptake, the drug was released by disassembly of the gold nanoparticle cluster into single gold nanoparticles in response to the pH decrease in the late endosome. Furthermore, the antiapoptotic Bcl-2 protein was down-regulated by the antisense-modified gold nanoparticles; thus, drug-mediated apoptosis was significantly accelerated by sensitizing the cancer cells to the drug. Our size-tunable clustered nucleic acid-grafted gold nanoparticles provide tumor homing in the blood circulation and are thus a potential multifunctional therapeutic agent *in vivo* as well as *in vitro*.

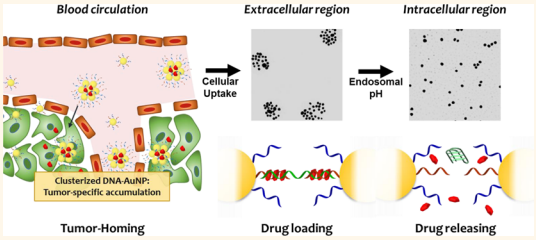

KEYWORDS: DNA nanotechnology · gold nanoparticle · drug delivery · i-motif · antisense

To date, polymeric and metallic nanoparticles have been utilized as DNA or drug delivery carriers, and they have shown different tumor targeting abilities depending on their size.[1−3] Nanoparticles sized less than 20 nm can extravasate from both leaky blood vessels in tumorous regions as well as normal blood vessels, resulting in low tumor-specific accumulation. In contrast, nanoparticles sized greater than 300 nm are easily eliminated by phagocytosis and hardly extravasate from even tumor blood vessels. Therefore, nanoparticles in the size range of 50−200 nm are highly recommended for tumor accumulation by the enhanced permeation and retention (EPR) effect.[4−7] Another critical factor for drug efficacy is rapid responsiveness to the cellular environment and subsequent drug release after internalization into cells.[8−10] After nanoparticles enter tumor cells, they should degrade to prevent cytotoxicity, followed by the release of their cargo, such as DNA or drugs. Therefore, clustered particles in which several small nanoparticles are assembled together for higher tumor accumulation and longer blood circulation should be disassembled into small nanoparticles after cellular uptake for low toxicity and efficient drug release.

Recently, metal nanoparticles modified with nucleic acids on their surface have attracted attention in the fields of biosensors,[11,12] gene delivery,[13−16] and structure formation[17−20] because of their unique properties. In particular, densely packed oligodeoxynucleotides (ODNs) on the nanoparticles recruit large amounts of counterions, thus providing intracellular stability by protecting the ODNs from enzymatic degradation in serum.[21] The remarkable cellular uptake and gene silencing ability of these nanoparticles without the help of cationic carriers suggest that they may be used as effective delivery agents.[13−16,22] Moreover, these nanoparticles are also utilized as building blocks for nanostructure formation.[17−20] Nucleic acids grafted on the surface enable the formation of a programmable and predictable self-assembled structure.[23−26] These ODN-based structural features can be used to induce the assembly of nanoparticles into clusters or disassembly into single nanoparticles through DNA hybridization.[27−29]

* Address correspondence to wjkim@postech.ac.kr.

Received for review June 20, 2014 and accepted September 3, 2014.

Published online September 03, 2014
10.1021/nn503349g

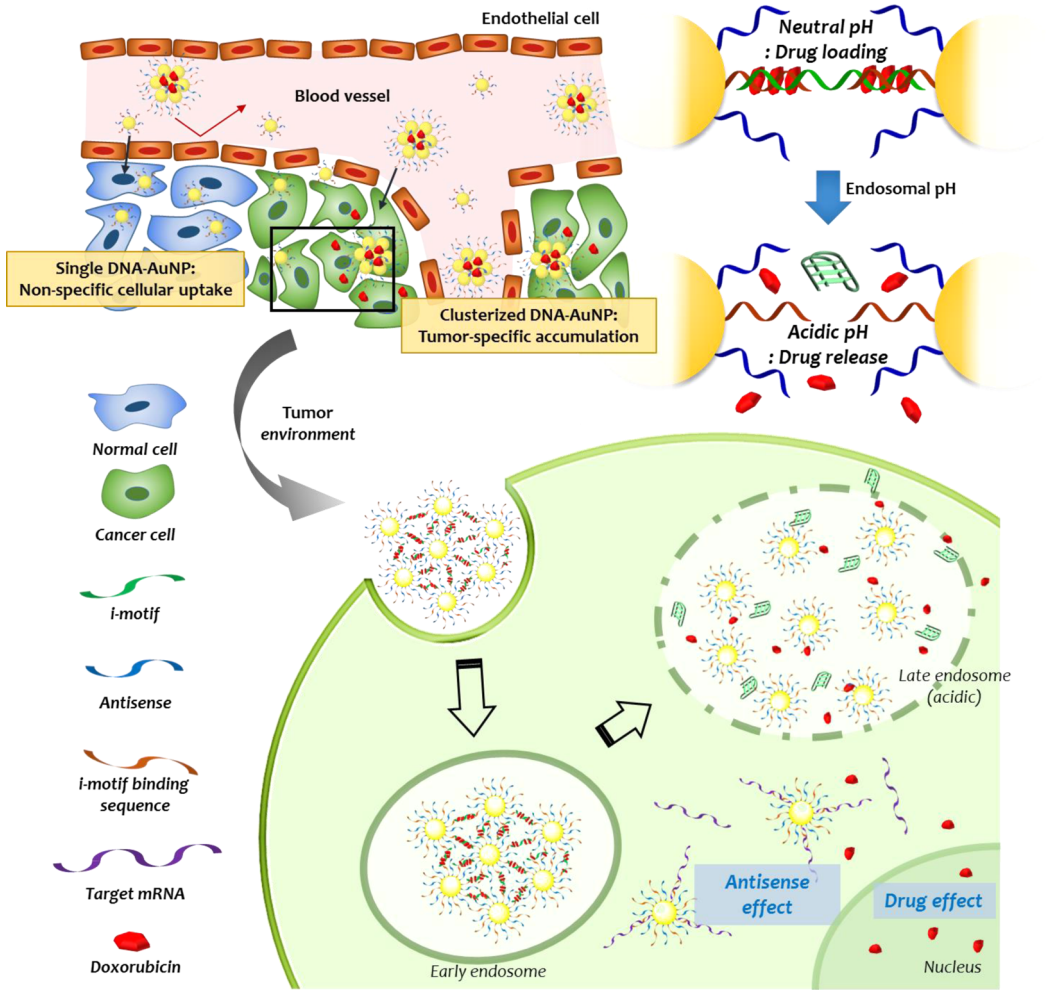

Figure 1. Schematic illustration of tumor accumulation of cAuNPs and subsequent cellular uptake for effective delivery of drug and antisense by intracellular pH stimulation.

In particular, the assembly and disassembly of nanoparticles can be controlled by modulating the hybridization stability between ODNs. Compared with large nanoparticles modified with ODNs, clustering of several small nanoparticles modified with ODNs provides a larger surface area for further functionalization. Furthermore, the duplex structure of ODNs can be used to load intercalative anticancer drugs such as doxorubicin (DOX), and hence, it can be used as a drug loading cargo.[30−32]

Two of the largest challenges in current drug delivery are multidrug resistance in cancer cells and adverse side effects. In particular, in cancer cells, the antiapoptotic Bcl-2 protein family inhibits the apoptosis of cancer cells by blocking the transcription of proapoptotic proteins such as cytochrome *c* and its downstream caspase cascade proteins. Therefore, to maximize drug efficiency and overcome drug resistance, the strategy of simultaneous antiapoptotic gene downregulation and drug treatment has been introduced.[33−35] In the present study, gold nanoparticles (AuNPs) were utilized as a template for ODN grafting. For higher tumor targeting efficiency, small single gold nanoparticles (sAuNPs) are clustered into size-tunable large clusters (cAuNPs) *via* hybridization with i-motif. The clusters can be disassembled into sAuNPs in response to the pH decrease after cellular uptake, followed by the release of antisense ODNs and anticancer drugs from sAuNPs.

We focused on the intracellular pH changes after endocytosis that releases the drug into the intracellular region *via* disassembly of the cluster.[36−38] For the construction of a multifunctional cAuNP vehicle, a sophisticated design was employed. The surface of AuNPs (~13 nm) was modified with two types of ODN, i-motif binding ODN (iBO, partially complementary to the i-motif) and bcl-2 antisense ODN. The cytosine (C)-rich i-motif sequence, which forms a unique tetrameric structure in acidic pH by partial hybridization of C and protonated C, was designed as a linker for clustering of sAuNPs (Figure 1).[39,40] Addition of the i-motif into complementary iBO-sAuNPs caused sAuNPs to cluster by partial hybridization of i-motif and iBO-sAuNPs at neutral pH. In acidic pH after cellular uptake, however, partial hybridization between i-motif occurred and iBO-sAuNPs dissociated, resulting in disassembly of clusters and enhanced exposure of

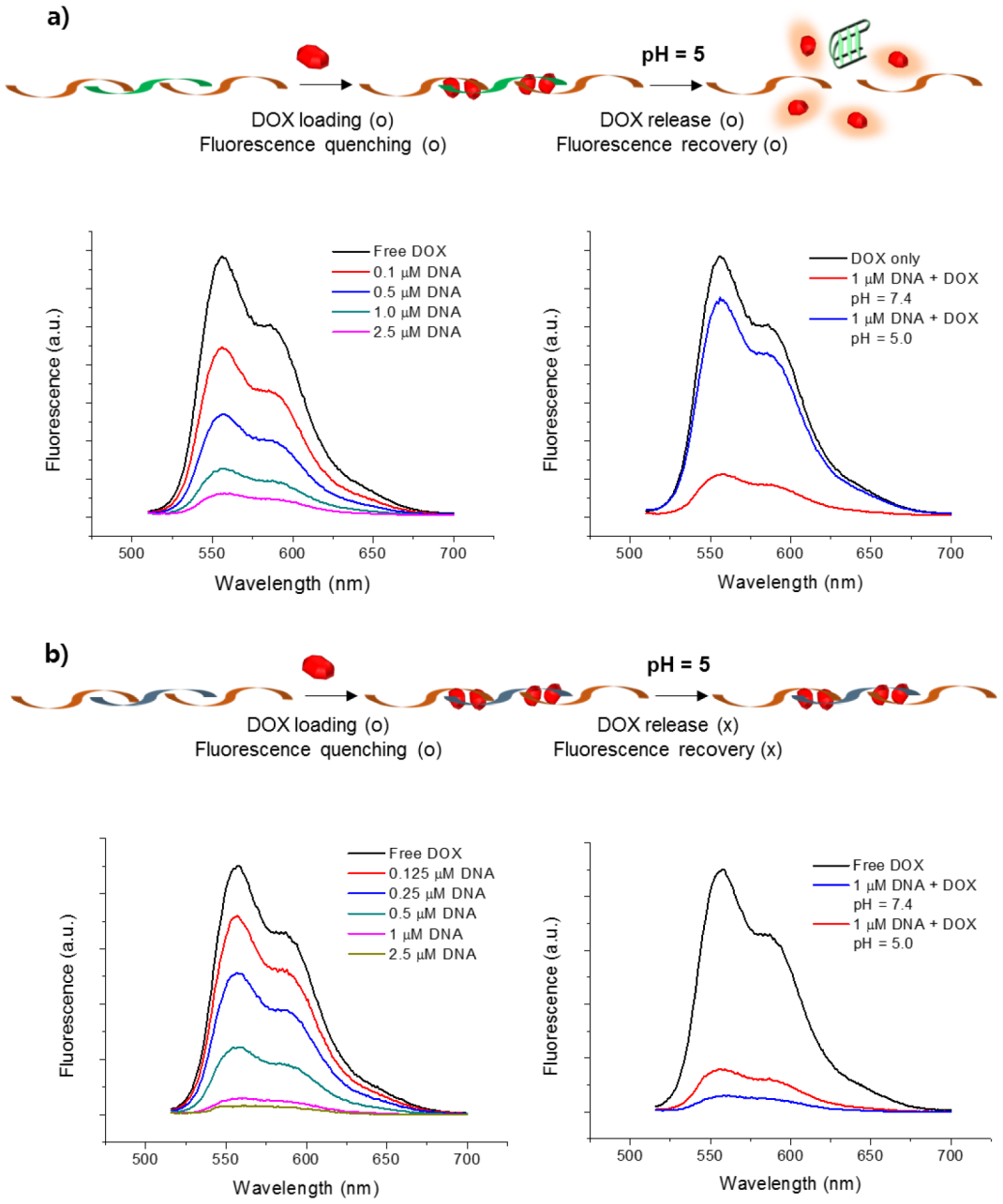

Figure 2. DOX loading and release profile based on ODN hybridization. (a) DOX loading and release using the pH-sensitive i-motif DNA sequence. The fluorescence intensity of DOX (5 μM) decreased gradually with increased DNA concentration and recovered on addition of HCl. (b) DOX loading and release using a pH-insensitive control DNA sequence.

antisense ODNs to mRNA. During the duplex formation between the i-motif and iBO-sAuNPs, the anticancer drug DOX was loaded into duplex base pairs by intercalation. The loaded DOX was expected to be released from the clusters by dissociation of the i-motif and iBO-sAuNPs at intracellular acidic endosomal pH. This multifunctional AuNP-based cluster can function inside the cell as a highly effective drug delivery carrier, as supported by the drug-sensitizing effect of the antisense ODN. In addition, the clustering of sAuNPs by i-motif increases the accumulation of AuNPs in the tumor region specifically *via* the EPR effect (Figure 1).

RESULTS AND DISCUSSION

pH-Sensitive Drug Loading and Release. The cytosine-rich i-motif sequence and iBO sequence were designed at each orientation (Table S1, Supporting Information). Prior to conjugation of ODN to AuNPs, the hybridization of the binding sequence and i-motif was confirmed by 12% polyacrylamine gel electrophoresis (PAGE) to verify the DNA assembly based on hybridization (Figure S1). In the hybridized partial-duplex structure at neutral pH, DOX was loaded on the duplex efficiently, and it was rapidly released at acidic pH through formation of the i-motif structure. The loading and release of DOX were monitored by quenching and

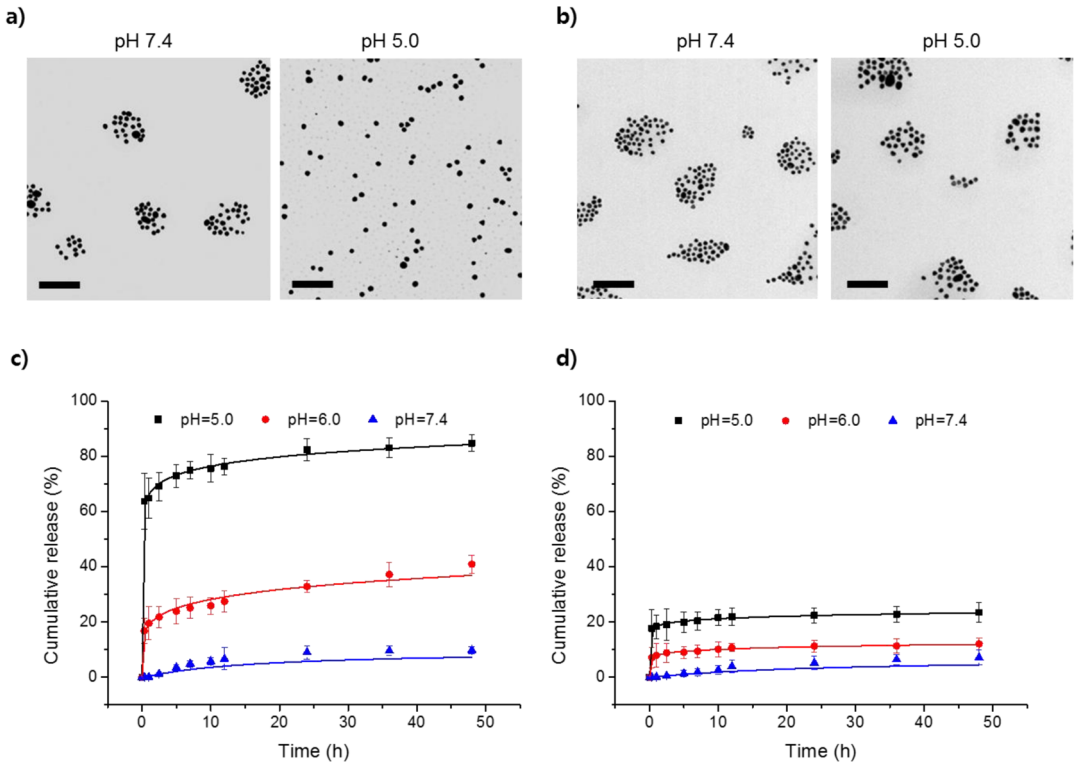

Figure 3. Assembly and disassembly of AuNPs and DOX release modulated by pH-sensitive i-motif or a control DNA sequence. (a, b) TEM image of AuNPs with the pH-sensitive i-motif (iBO-cAuNPs) (a) and pH-insensitive control sequence (cBO-cAuNP) (b) at pH 7.4 and pH 5.0. The scale bar represents 200 nm. (c, d) Release profile of intercalated DOX from iBO-cAuNPs (c) and cBO-cAuNPs (d) at various pH values.

recovery of the intrinsic fluorescence of DOX (Figure 2). Compared with the pH-sensitive i-motif, the pH-insensitive random sequence (control sequence) and its complementary sequence (control binding ODN, cBO) demonstrated negligible drug release at acidic pH. This result demonstrates that the i-motif sequence is a linker for the structural assembly and disassembly of ODNs with drug cargo depending on the pH change.

pH-Sensitive AuNP Assembly and Disassembly. To prepare pH-responsive AuNPs, the surface of the AuNPs was modified with high number of ODN strands (approximately 100 strands of iBO and antisense) by a salt aging process (Figure S1).[8−10] The clustering of AuNPs was performed by adding the i-motif and subsequent annealing with iBO-sAuNPs.[41−43] The i-motif-mediated clustering of AuNPs (iBO-cAuNPs) with an average size of 150 nm was confirmed at neutral pH by transmission electron microscopy (TEM). The iBO-cAuNPs disassembled into sAuNPs by forming i-motif tetrameric structure in acidic conditions (pH = 5.0) as observed in Figure 3a. As a control, AuNPs modified with the pH-insensitive cBO sequence were synthesized and cluster formation was monitored. Similarly to the pH-sensitive sequence, cBO-mediated sAuNP cluster (cBO-cAuNPs) formation was observed at neutral pH on addition of a control complementary sequence. However, acidic pH did not induce the disassembly of cBO-cAuNPs as observed by TEM imaging (Figure 3b). These results imply that i-motif-guided clustering induces dynamic disassembly of AuNP clusters at acidic pH, which is similar to the intracellular endosomal pH inside cells.

As mentioned above, hybridization of the i-motif and iBO-sAuNPs generates a duplex structure, possessing the drug-loading capability of a cluster. Up to 500 DOX molecules per one AuNP were loaded into the cAuNPs (Figure S4a). We utilized these cAuNPs with 500 DOX molecules per AuNP for further drug release and efficacy experiments. The high drug-loading capability might result from the high number of nucleic acids on the surface of the AuNPs. Additionally, because iBO-cAuNPs disassemble at acidic pH, they release DOX (~90%) from iBO-cAuNPs by forming separate AuNPs and i-motif tetraplexes (Figure 3c). However, at neutral pH, less than 10% of the drug was released from the clusters. In contrast, in the case of pH-insensitive cBO-cAuNPs, only a low amount of DOX was released even at acidic pH (less than 30%) because the cAuNPs could not respond to the pH change (Figure 3d).

Evaluation of *in Vitro* Drug Effect. We next investigated the intracellular performance of AuNP clusters as an effective and multifunctional drug delivery carrier. Bcl-2 antisense, which was conjugated onto the AuNPs, was able to bind the target mRNA with high sequence specificity and knock down Bcl-2 protein expression. As shown in Western blotting (Figure 4a), Bcl-2 protein

expression was significantly blocked in the group treated with bcl-2 antisense-modified AuNP clusters (as-iBO-cAuNPs), whereas a strong band was observed in cells treated with scrambled-sequence-modified AuNP clusters (sc-iBO-cAuNPs), implying a lack of protein down-regulation. This result indicates that as-iBO-cAuNPs function inside cells as an antisense therapeutic agent with high sequence specificity.

It is also expected that the drug effect toward cancer cells will be maximized when multidrug resistance is alleviated by antisense treatment. To verify this strategy, four different cell lines, HeLa (human cervical cancer cell), A549 (human lung adenocarcinoma epithelial cell), MCF-7 (human breast adenocarcinoma cell), and drug-resistant HCT-8 (human colon carcinoma cell) were treated with DNA-grafted AuNPs and doxorubicin (DOX), followed by monitoring of cell viability by the (3-(4,5-dimethylthiazol-2-yl)-2,5-diphenyltetrazolium bromide) MTT assay (Figure 4b,c; Supporting Information Figure S5). As expected, the viability of cells treated with bcl-2 antisense-modified iBO-cAuNPs (as-iBO-cAuNP-DOX) was significantly decreased in all four cell lines. Even in the drug-resistant HCT-8 cell line, as-iBO-cAuNP-DOX showed a significantly higher drug effect than free DOX, possibly because of the synergistic effect of antisense and alleviating drug resistance. In addition, the cell viability of the group treated with scrambled-sequence antisense-modified i-motif AuNPs (sc-iBO-cAuNP-DOX) was lower than that of cells treated with free DOX; therefore, the pH-responsive activity of iBO-AuNPs plays a crucial role in the enhancement of drug delivery efficiency. In contrast, in a control group treated with AuNPs modified by pH-insensitive ODNs and antisense (as-cBO-cAuNP-DOX), the anticancer effect was not significant. This result indicates that only a low amount of the drug was released by passive drug release from pH-insensitive AuNPs clusters; these findings agreed well with the drug release profile *in vitro* (Figure 3c,d). In addition, cytotoxicity of ODN-modified AuNPs without DOX (as-iBO-cAuNP or sc-iBO-cAuNP) was not observed, implying that the antisense only functions as a sensitizer to enhance the drug effect.

Intracellular Behavior of pH-Sensitive cAuNPs. The intracellular function of AuNP clusters after cellular uptake was monitored by confocal laser scanning microscopy (CLSM) using the fluorescence of DOX. In the case of pH-sensitive as-iBO-cAuNP-DOX, a strong fluorescence signal was observed in the nucleus and in the cytoplasm, whereas the pH-insensitive as-cBO-cAuNP-DOX showed very weak DOX fluorescence (Figure 5a, b). Quantification of drug release using the fluorescence signal intensity revealed that DOX release was approximately 2.3-fold higher from the pH-sensitive as-iBO-cAuNP-DOX than from the pH-insensitive as-cBO-cAuNP-DOX (Figure 5c). Therefore, the intracellular endosomal pH triggered the disassembly of as-iBO-cAuNP-DOX, inducing extensive drug release inside the cell after endocytosis. To verify the crucial role of endosomal pH, cells were treated with bafilomycin A1 (Baf A1), which inhibits endosomal acidification, and evaluation of the intracellular trafficking of the AuNP clusters revealed low drug release efficiency. From these results, we consider that higher drug effect observed for pH-sensitive i-motif-mediated AuNPs clusters resulted from efficient drug release triggered by acidic endosomal pH (Figure S6).

The detailed dynamic movements of pH-sensitive iBO-AuNPs clustering inside cells were further studied using TEM analysis at different time intervals (Figure 6).

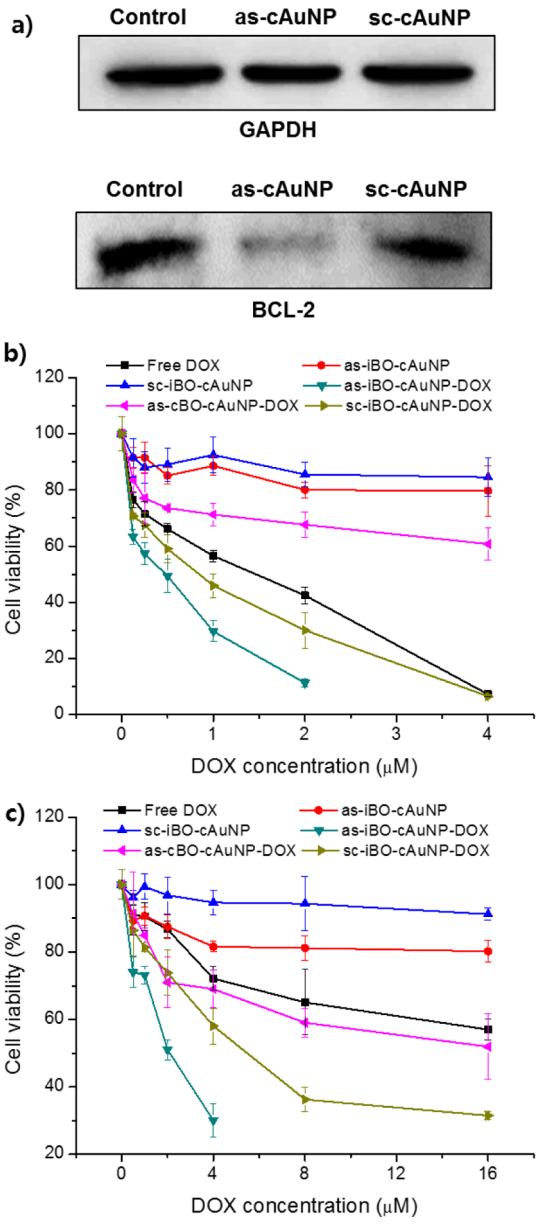

Figure 4. Assessment of *in vitro* drug effect. (a) Western blot analysis to monitor intracellular protein level after treatment with bcl-2 antisense-grafted cAuNPs (as-cAuNPs) and scrambled DNA-grafted cAuNPs (sc-AuNPs). (b, c) Cell viability testing for HeLa cells (b) and drug-resistant HCT-8 cells (c) treated with each type of AuNP.

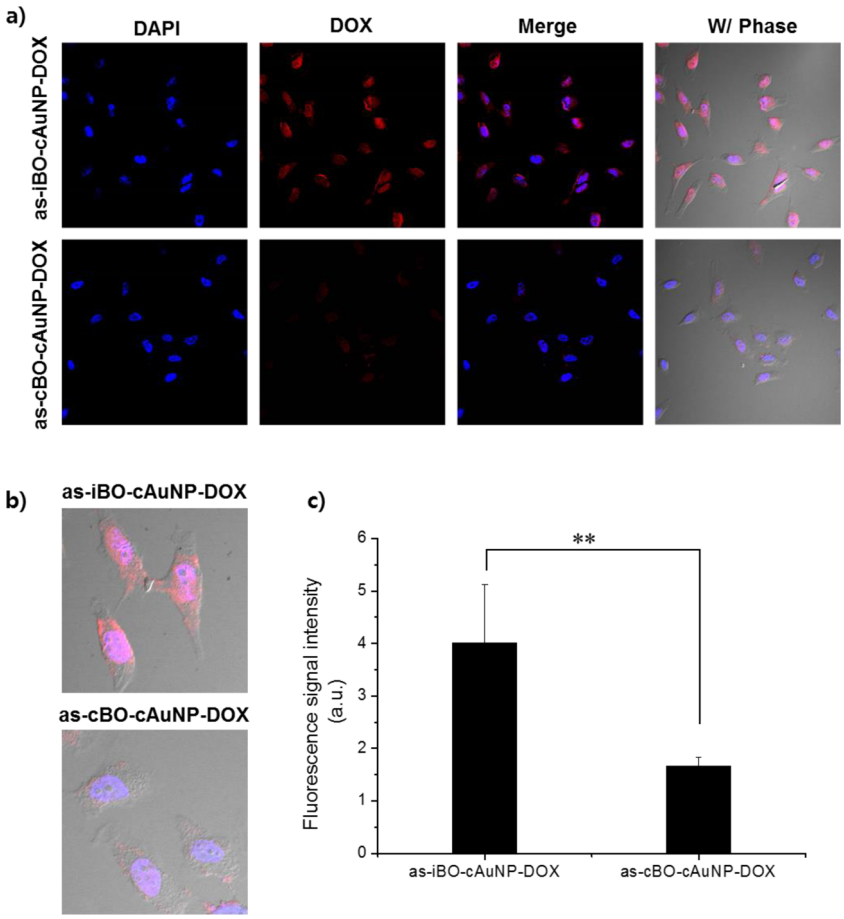

Figure 5. Intracellular DOX-releasing behavior of AuNP clusters. (a) Confocal laser scanning microscopy images of HeLa cells treated with pH-sensitive as-iBO-cAuNP-DOX and pH-insensitive as-cBO-cAuNP-DOX. Nuclei were stained with DAPI (blue). Red fluorescence shows the released DOX. (b) Magnified images. (c) Quantitative fluorescence signal intensity graph. Signal intensity is defined as the total integration of the DOX signal divided by cell numbers. Data represent the mean ± SD ($n = 5$, $^{**}P < 0.01$).

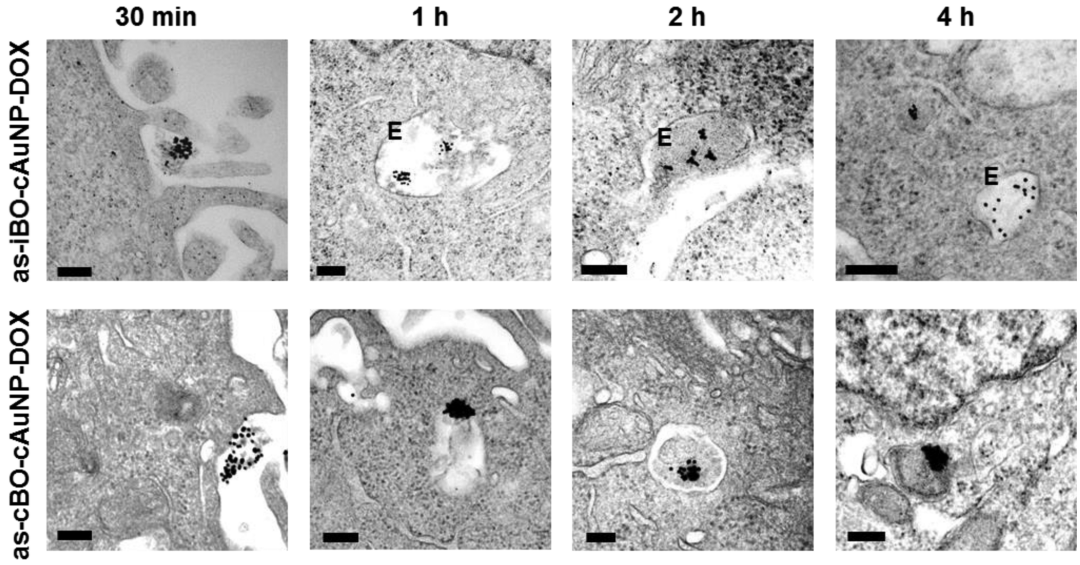

Figure 6. TEM images of HeLa cells treated with pH-sensitive iBO-cAuNPs and pH-insensitive cBO-cAuNPs for different time intervals. "E" represents the endosome compartment in the cell. The scale bar represents 200 nm.

AuNP clusters were taken up by endocytosis at the very early stage of 30 min. Whole-cell TEM imaging confirmed that high numbers of AuNP clusters were internalized into the cell (Figure S8). Before endosome maturation at 1 h, as-iBO-cAuNPs remained without being disassembled into sAuNPs. With an incubation

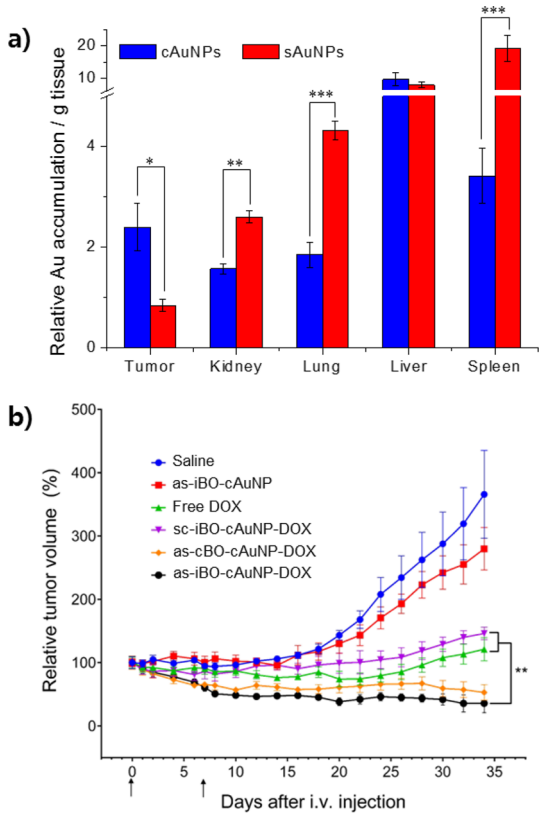

Figure 7. (a) Quantitative analysis of AuNP distribution in each organ after treatment with sAuNPs or cAuNPs using ICP-MS (n = 4). The results represent the mean ± SE of relative accumulation with respect to gram of tissues. (b) Antitumor activity in A549-bearing nude mice. Each sample was administrated intravenously at a total DOX dose of 5 mg/kg on day 0 and day 7, as indicated by the arrows. Each group contains 7 mice (n = 7), and tumor volumes are summarized as mean ± SE (*P < 0.05, **P < 0.01, ***P < 0.001).

time of 2 h, partial disassembly of as-iBO-cAuNPs into smaller as-iBO-cAuNPs composed of 3−5 sAuNPs was observed, indicating only partial i-motif formation at a mildly low pH (pH 6−6.5). At the late endosome stage at 4 h, which is sufficiently acidic to trigger i-motif formation, as-iBO-cAuNPs were completely disassembled into sAuNPs. In contrast, no dynamic function of as-cBO-cAuNPs with the pH-insensitive control sequence was observed. This TEM result clearly supports the dynamic function of AuNPs with a pH-sensitive i-motif structure responding to intracellular pH after endocytosis.

***In Vivo* Tumor-Homing and Antitumor Effect.** Next, we verified our concept in an *in vivo* anticancer experiment using AuNP clusters. As reported in previously published literature, even though the high internalization of DNA-grafted AuNPs into the cell and the excellent gene regulation are rather promising for *in vitro* applications, systemic applications of DNA-grafted AuNPs are not recommended because of high cellular uptake into the nontumorous region.[1,44−46] Therefore, clustering of AuNPs to an appropriate size can induce tumor-specific accumulation by the EPR effect with low accumulation in nontumorous organs. After tumor accumulation, the clustered AuNPs would be disassembled into small, single AuNPs that recover their original function.

Prior to the tumor growth inhibition experiment, to verify the beneficial effect of clustering small sAuNPs, an *in vivo* biodistribution assay was performed after systemic injection of cAuNPs or sAuNPs, followed by examination of AuNP accumulation using inductively coupled plasma mass spectrometry (ICP-MS). As shown in Figure 7a, the cAuNP-treated group showed 2.5-fold higher tumor accumulation and lower accumulation in other organs compared with the sAuNP-treated group, except in the liver, possibly because of the EPR effect.[13−16] This finding indicates that higher tumor-specific accumulation and lower accumulation in nontumorous organs were achieved using clustered sAuNPs.

We then evaluated the antitumor effect of AuNP clusters having antisense and DOX as synergistic therapeutics. Tumor volume was measured in an A549-bearing mouse xenograft model. The as-iBO-cAuNP-DOX-treated group showed significant and sustained tumor inhibition when compared with the free DOX-treated group or scrambled AuNP cluster (sc-iBO-cAuNP-DOX). These results indicate that the bcl-2 antisense sensitized the tumor cells toward DOX; thus, the drug effect was maximized and sustained relative to that of free DOX or sc-iBO-cAuNP-DOX (Figure 7b; Supporting Information Figures S9, S10). The efficient inhibition of tumor growth by as-iBO-cAuNP-DOX was also confirmed by a bioimaging assay using A549 cells expressing luciferase; the findings agreed with those of a previous tumor inhibition assay (Figure S11).

CONCLUSION

In conclusion, our study demonstrated the design of tumor-homing DNA-grafted AuNP clusters and evaluated their function as a pH-responsive drug delivery system. Tunable clustering of small sAuNPs by i-motif ODNs provided higher tumor specificity and efficient drug release. Our precisely designed nanostructure showed a synergistic effect for the antisense and anticancer drug and thus may overcome current impediments to using small nanoparticles in systematic administration.

EXPERIMENTAL SECTION

Materials. Gold chloride hydrate ($HAuCl_4$), sodium citrate tribasic dehydrate (NaCit), and tris(2-carboxyethyl) phosphine hydrochloride (TCEP) were obtained from Sigma-Aldrich Co. (St. Louis, MO). All commercial reagents were used without further purification. All oligonucleotide sequences were purified by HPLC and purchased from Bioneer Corp. (Daejeon, South Korea). The detailed information on ODN sequences are listed in Table S1.

Synthesis of Citrated-Capped Gold Nanoparticles (Au-cit). Au nanoparticles were synthesized by reduction of $HAuCl_4$ at high temperature in the presence of citrate ion. $HAuCl_4$ solution (30 mL, 1.47 mM in ultrapure water) was prepared at 120 °C. After 15 min, 600 μL of citrate solution (0.34 M in ultrapure water) was added into the $HAuCl_4$ solution. After the color of solution changed from light yellow to dark red, the solution was stored at 4 °C without any further purification.

Modification of Gold Surface with Nucleotides. The thiol modified ODN (10 nmol in 500 μL acetate buffer, pH = 5.5) was activated by 2 μL, 10 mM TCEP for 2 h at room temperature and purified using NAP-25 column. The activated ODNs (iBO and bcl-2 antisense) were added to AuNPs (13 nm) at a molar ratio of 1:150. The initial mixture was incubated 3 days with salt aging process from 0.1 M NaCl to 0.3 M NaCl. The mixture was further incubated 24 h to complete the oligonucleotide functionalization process. The final products were centrifuged (16 100 rcf, 30 min) and washed twice with tris-acetate buffer with 0.1 M NaCl (pH = 8.2) and then stored in tris-acetate buffer with 0.3 M NaCl (pH = 8.2).

Clustering of AuNPs and Drug Loading. Nucleotide-modified AuNPs were diluted to less than 1 nM concentration. pH-responsive i-motif sequence was added into the sAuNPs as 100 equiv per 1 AuNP and gently mixed. Then, the mixture was incubated at 2 °C for 30 min. Longer incubation can cause severe aggregation. The solution was centrifuged (10 000 rcf, 30 min) for the separation of cAuNPs. All of the experiments were conducted in tris-acetate buffer with 0.3 M NaCl and 10 mM Mg. The drug loading was followed by AuNPs clustering. In a purified and diluted cAuNPs, DOX was added until 500 mol equiv per 1 AuNP and gently mixed, followed by overnight incubation. More than 600 equiv of DOX induced nonspecific aggregation. The centrifugation (10 000 rcf, 30 min) of DOX-loaded cAuNPs was conducted to purify the sample, and the fluorescence of supernatant was measured to verify the DOX loading efficiency. In a supernatant solution, no fluorescence of DOX was observed in 500 equiv of DOX added to cAuNPs means almost all drugs are loaded.

Drug Release Test. The fluorescence of DOX (ex. 495 nm, em. 555 nm in buffer or em. 595 nm in serum containing media) was measured in different concentration at various pH to obtain calibration curves. HCl (1 M) solution was added to DOX-loaded cAuNPs, followed by centrifugation (16 100 rcf, 15 min). The fluorescence of supernatant was measured and quantified by the calibration curve. The amount of drug release was calculated as [(amount of drug release)/(amount of drug loading) × 100].

Cell Culture. HeLa (human cervical cancer cells) and NIH/3T3 (mouse embryo fibroblast cells) were cultured in Dulbecco's modified Eagle's medium (DMEM, Hyclone). A549 (human lung adenocarcinoma epithelial cells) and MCF-7 (human breast adenocarcinoma cells) were cultured in Roswell Park Memorial Institute medium (RPMI-1640, Hyclone). Each media contained 10% fetal bovine serum (FBS, Hyclone), 100 U/mL penicillin, and 100 μg/mL streptomycin and was incubated at 37 °C in a 5% CO_2 humidified incubator.

Cell Viability Test. *In vitro* cytotoxicity of as-iBO-cAuNP, sc-iBO-cAuNP, free DOX, sc-iBO-cAuNP-DOX, as-iBO-cAuNP-DOX, and as-nBO-cAuNP-DOX was evaluated using 3-(4,5-dimethylthiazol-2-yl)-2,5-diphenyltetrazolium bromide (MTT) in HeLa, NIH/3T3, A549, and MCF-7 cells. Cells were seeded on 96-well culture plate at an initial density of 6×10^3 cells/well and incubated for 24 h at 37 °C in 5% CO_2 humidified incubator. Cells were treated with each sample and incubated in culture media for 48 h and 20 μL of MTT solution (5 mg/mL) was treated and incubated further 4 h. The medium was then removed, and 200 μL of dimethyl sulfoxide (DMSO) was added to make the formazan salt solution. After the transfer of 100 μL aliquots in each well, the absorbance at 570 nm was measured using a microplate spectrofluorometer (Victor3 V Multilabel Counter, PerkinElmer, Wellesley, MA).

Western Blot Analysis. HeLa cells were seeded in a 6-well culture plate at an initial density of 5×10^5 cells/well and incubated for 24 h at 37 °C in a 5% CO_2 humidified incubator. Cells were treated with samples and incubated for 24 h in culture media and lysed to get whole protein. The total protein concentration of cells was measured using the Bradford protein assay. The GAPDH and BCL-2 protein were separated by 12% SDS-PAGE and transferred to Millipore PVDF membranes. Membranes were blocked with Blocking solution (Invitrogen) and incubated with anti-GAPDH and anti-BCL-2 (Sigma, St. Louis, MO) at 4 °C overnight. The detection of antibodies was conducted with horseradish peroxidase (HRP)-conjugated secondary antibody and the Novex ECL HRP chemiluminescent substrate reagent kit (Invitrogen). The electrochemiluminescence was measured using a FUJI LAS 4000 instrument (Fujifilm, Japan).

Confocal Laser Scanning Microscopy Analysis. HeLa and A549 cells were seeded at an initial density of 2×10^4 cells/well in a 12-well culture plate over glass coverslips. After 24 h incubation in a 5% CO_2 humidified incubator, cells were treated with samples in culture media. After 2 h incubation, cellular uptake was quenched by adding cold DPBS, followed by washing two times with DPBS. After washing, cells were fixed with 4% paraformaldehyde overnight at 4 °C. Cells on the coverslip were mounted in Vectashield antifade mounting medium (Vector Laboratories), and the image was obtained with an Olympus FV-1000 instrument and analyzed with Olympus Fluoview version 1.5 viewer software.

Transmission Electron Microscopy (TEM). The size and morphology of AuNPs were obtained using TEM (JEOL JEM-1011, Japan) with an accelerating voltage of 40−100 kV. For cellular TEM images, HeLa cells were fixed in modified Karnovsky's fixative (2.5% glutaraldehyde and 2% paraformaldehyde ini 0.1 mM cacodylate buffer, with 2.5 mM calcium chloride), stained with saturated uranyl acetate, followed by dehydration using ethanol and infiltration with Spurr's plastic. The infiltrated specimen was cut into light-gold-colored ultrathin sections in 90 nm thickness and stained on the grid with uranyl acetate and Raynold's lead citrate.

***In Vivo* Experiment.** All animal experiments were approved by the Postech Biotech Center Ethics Committee. Cells (1×10^7 A549 cells) were inoculated subcutaneously (s.c.) into the flank of each female Balb/c-nu/nu mice weighing 17 ± 2 g. After the average tumor volume reached 100 mm^2, the mice were randomly divided into six groups (seven mice per group) and treated with 100 μL of physiological saline, as-iBO-cAuNP, free DOX, sc-iBO-cAuNP-DOX, as-iBO-cAuNP-DOX, and as-nBO-cAuNP-DOX twice (2 mg/kg DOX at day 12 and 3 mg/kg DOX at day 19 after inoculation), intravenously (i.v.). The antitumor effect against the growth of A549 was measured by tumor volume. Each tumor was measured in two dimensions using an electronic caliper every other day. The recorded measurements were converted to volume using the formula for a prolate ellipsoid: [tumor volume = $(ab^2/2)$], where a is the longest and b is the shortest dimension. The tumor growth was monitored until the tumor was ulcerated, at which time the mice were sacrificed (on day 35 post sample injection). All results are expressed as mean ± SE. To demonstrate statistical differences, one-way or two-way ANOVA was performed ($p < 0.05$), and all of the results were analyzed using the software GraphPad Prism 6 for Windows. For imaging experiment, luciferase (LUC) expressing A549 cells (A549-LUC) were subcutaneously injected into the female Balb/c-nu/nu mice (1×10^7 cells/mouse). The mice were treated with saline, as-iBO-cAuNP, free DOX, sc-iBO-cAuNP-DOX, as-iBO-cAuNP-DOX, and as-nBO-cAuNP-DOX. The luciferin substrate was injected intraperitoneally (i.p.) just before every *in vivo* imaging assay, and the luminescence of tumor cells was monitored after 10 min. The image was obtained and analyzed with an IVIS spectrum small-animal *in vivo* imaging system (Califer Lifesciences, Hopkinton, MA).

Inductively Coupled Plasma Mass Spectrometry (ICP-MS). A549-bearing nude mice xenograft was utilized for ICP-MS analysis. The mice were randomly divided into two groups (four mice per group) and treated with 100 μL of as-iBO-cAuNPs and as-iBO-sAuNPs. After 24 h, all mice were sacrificed and each organ was separated, including blood. Each sample was dried completely, and the weight was measured. Nitric acid was used to treat each organ, and the temperature was elevated up to 210 °C to totally digest organic molecules in tissues. Several heating and cooling process were done, and the digestion was ended when the solution became totally transparent. AuNP standard was also prepared to obtain the calibration curve. The measurement was conducted

using a NexION 300 ICP-MS spectrometer (PerkinElmer, Wellesley, MA). The amount of accumulated Au was calculated as [existing gold in tissue/whole amount of injected gold].

Conflict of Interest: The authors declare no competing financial interest.

Acknowledgment. This work was supported by the Research Center Program of IBS (Institute for Basic Science) in Korea (CA1203-02). We specially thank to Dr. W. Y. Song for assistance in the ICP-MS analysis.

Supporting Information Available: ODN sequences; Confirmation of DNA hybridization; Quantification of ODN strands in AuNPs; pH-dependent hydrodynamic measurement; Cell-line dependency of drug loaded AuNPs cluster; pH-dependent drug release and efficacy inside the cell; *ex vivo* tumor weight measurement after injection; *in vivo* monitoring and imaging of drug loaded AuNPs cluster. This material is available free of charge *via* the Internet at http://pubs.acs.org.

REFERENCES AND NOTES

1. Cho, K. J.; Wang, X.; Nie, S. M.; Chen, Z.; Shin, D. M. Therapeutic Nanoparticles for Drug Delivery in Cancer. *Clin. Cancer Res.* **2008**, *14*, 1310–1316.
2. Huang, K. Y.; Ma, H. L.; Liu, J.; Huo, S. D.; Kumar, A.; Wei, T.; Zhang, X.; Jin, S. B.; Gan, Y. L.; Wang, P. C.; *et al.* Size-Dependent Localization and Penetration of Ultrasmall Gold Nanoparticles in Cancer Cells, Multicellular Spheroids, and Tumors *in Vivo*. *ACS Nano* **2012**, *6*, 4483–4493.
3. Maeda, H.; Nakamura, H.; Fang, J. The EPR Effect for Macromolecular Drug Delivery to Solid Tumors: Improvement of Tumor Uptake, Lowering of Systemic Toxicity, and Distinct Tumor Imaging *in Vivo*. *Adv. Drug Delivery Rev.* **2013**, *65*, 71–79.
4. Albanese, A.; Tang, P. S.; Chan, W. C. The Effect of Nanoparticle Size, Shape, and Surface Chemistry on Biological Systems. *Annu. Rev. Biomed. Eng.* **2012**, *14*, 1–16.
5. De Jong, W. H.; Hagens, W. I.; Krystek, P.; Burger, M. C.; Sips, A. J.; Geertsma, R. E. Particle Size-Dependent Organ Distribution of Gold Nanoparticles after Intravenous Administration. *Biomaterials* **2008**, *29*, 1912–1919.
6. Kim, J.; Park, J.; Kim, H.; Singha, K.; Kim, W. J. Transfection and Intracellular Trafficking Properties of Carbon Dot-Gold Nanoparticle Molecular Assembly Conjugated with PEI-pDNA. *Biomaterials* **2013**, *34*, 7168–7180.
7. Kim, H.; Lee, D.; Kim, J.; Kim, T. I.; Kim, W. J. Photothermally Triggered Cytosolic Drug Delivery *via* Endosome Disruption Using a Functionalized Reduced Graphene Oxide. *ACS Nano* **2013**, *7*, 6735–6746.
8. Cutler, J. I.; Auyeung, E.; Mirkin, C. A. Spherical Nucleic Acids. *J. Am. Chem. Soc.* **2012**, *134*, 1376–1391.
9. Giljohann, D. A.; Seferos, D. S.; Daniel, W. L.; Massich, M. D.; Patel, P. C.; Mirkin, C. A. Gold Nanoparticles for Biology and Medicine. *Angew. Chem., Int. Ed.* **2010**, *49*, 3280–3294.
10. Macfarlane, R. J.; O'Brien, M. N.; Petrosko, S. H.; Mirkin, C. A. Nucleic Acid-Modified Nanostructures as Programmable Atom Equivalents: Forging a New "Table of Elements". *Angew. Chem., Int. Ed.* **2013**, *52*, 5688–5698.
11. Farokhzad, O. C.; Langer, R. Nanomedicine: Developing Smarter Therapeutic and Diagnostic Modalities. *Adv. Drug Delivery Rev.* **2006**, *58*, 1456–1459.
12. Rosi, N. L.; Mirkin, C. A. Nanostructures in Biodiagnostics. *Chem. Rev.* **2005**, *105*, 1547–1562.
13. Giljohann, D. A.; Seferos, D. S.; Patel, P. C.; Millstone, J. E.; Rosi, N. L.; Mirkin, C. A. Oligonucleotide Loading Determines Cellular Uptake of DNA-Modified Gold Nanoparticles. *Nano lett* **2007**, *7*, 3818–3821.
14. Giljohann, D. A.; Seferos, D. S.; Prigodich, A. E.; Patel, P. C.; Mirkin, C. A. Gene Regulation with Polyvalent siRNA-Nanoparticle Conjugates. *J. Am. Chem. Soc.* **2009**, *131*, 2072–2073.
15. Rosi, N. L.; Giljohann, D. A.; Thaxton, C. S.; Lytton-Jean, A. K.; Han, M. S.; Mirkin, C. A. Oligonucleotide-Modified Gold Nanoparticles for Intracellular Gene Regulation. *Science* **2006**, *312*, 1027–1030.
16. Cutler, J. I.; Zhang, K.; Zheng, D.; Auyeung, E.; Prigodich, A. E.; Mirkin, C. A. Polyvalent Nucleic Acid Nanostructures. *J. Am. Chem. Soc.* **2011**, *133*, 9254–9257.
17. Huo, F. W.; Lytton-Jean, A. K. R.; Mirkin, C. A. Asymmetric Functionalization of Nanoparticles Based on Thermally Addressable DNA Interconnects. *Adv. Mater.* **2006**, *18*, 2304–2305.
18. Xu, X. Y.; Rosi, N. L.; Wang, Y. H.; Huo, F. W.; Mirkin, C. A. Asymmetric Functionalization of Gold Nanoparticles with Oligonucleotides. *J. Am. Chem. Soc.* **2006**, *128*, 9286–9287.
19. Maye, M. M.; Nykypanchuk, D.; Cuisinier, M.; van der Lelie, D.; Gang, O. Stepwise Surface Encoding for High-Throughput Assembly of Nanoclusters. *Nat. Mater.* **2009**, *8*, 388–391.
20. Lim, D. K.; Jeon, K. S.; Kim, H. M.; Nam, J. M.; Suh, Y. D. Nanogap-Engineerable Raman-Active Nanodumbbells for Single-Molecule Detection. *Nat. Mater.* **2010**, *9*, 60–67.
21. Seferos, D. S.; Prigodich, A. E.; Giljohann, D. A.; Patel, P. C.; Mirkin, C. A. Polyvalent DNA Nanoparticle Conjugates Stabilize Nucleic Acids. *Nano Lett.* **2009**, *9*, 308–311.
22. Massich, M. D.; Giljohann, D. A.; Seferos, D. S.; Ludlow, L. E.; Horvath, C. M.; Mirkin, C. A. Regulating Immune Response Using Polyvalent Nucleic Acid-Gold Nanoparticle Conjugates. *Mol. Pharmaceutics* **2009**, *6*, 1934–1940.
23. Wu, C.; Han, D.; Chen, T.; Peng, L.; Zhu, G.; You, M.; Qiu, L.; Sefah, K.; Zhang, X.; Tan, W. Building a Multifunctional Aptamer-Based DNA Nanoassembly for Targeted Cancer Therapy. *J. Am. Chem. Soc.* **2013**, *135*, 18644–18650.
24. Zheng, J.; Zhu, G. Z.; Li, Y. H.; Li, C. M.; You, M. X.; Chen, T.; Song, E. Q.; Yang, R. H.; Tan, W. H. A Spherical Nucleic Acid Platform Based on Self-Assembled DNA Biopolymer for High-Performance Cancer Therapy. *ACS Nano* **2013**, *7*, 6545–6554.
25. Seeman, N. C.; Kallenbach, N. R. Design of Immobile Nucleic Acid Junctions. *Biophys. J.* **1983**, *44*, 201–209.
26. Yurke, B.; Turberfield, A. J.; Mills, A. P.; Simmel, F. C.; Neumann, J. L. A DNA-Fuelled Molecular Machine Made of DNA. *Nature* **2000**, *406*, 605–608.
27. Modi, S.; Swetha, M. G.; Goswami, D.; Gupta, G. D.; Mayor, S.; Krishnan, Y. A DNA Nanomachine that Maps Spatial and Temporal pH Changes Inside Living Cells. *Nat. Nanotechnol.* **2009**, *4*, 325–330.
28. Scheinberg, D. A.; Villa, C. H.; Escorcia, F. E.; McDevitt, M. R. Conscripts of the Infinite Armada: Systemic Cancer Therapy Using Nanomaterials. *Nat. Rev. Clin. Oncol.* **2010**, *7*, 266–276.
29. Surana, S.; Bhat, J. M.; Koushika, S. P.; Krishnan, Y. An Autonomous DNA Nanomachine Maps Spatiotemporal pH Changes in a Multicellular Living Organism. *Nat. Commun.* **2011**, *2*, 340.
30. Bagalkot, V.; Farokhzad, O. C.; Langer, R.; Jon, S. An Aptamer-Doxorubicin Physical Conjugate as a Novel Targeted Drug-Delivery Platform. *Angew. Chem., Int. Ed.* **2006**, *45*, 8149–8152.
31. Kim, D.; Jeong, Y. Y.; Jon, S. A Drug-Loaded Aptamer-Gold Nanoparticle Bioconjugate for Combined CT Imaging and Therapy of Prostate Cancer. *ACS Nano* **2010**, *4*, 3689–3696.
32. Xiao, Z. Y.; Ji, C. W.; Shi, J. J.; Pridgen, E. M.; Frieder, J.; Wu, J.; Farokhzad, O. C. DNA Self-Assembly of Targeted Near-Infrared-Responsive Gold Nanoparticles for Cancer Thermo-Chemotherapy. *Angew. Chem., Int. Ed.* **2012**, *51*, 11853–11857.
33. Chen, A. M.; Zhang, M.; Wei, D. G.; Stueber, D.; Taratula, O.; Minko, T.; He, H. X. Co-Delivery of Doxorubicin and Bcl-2 siRNA by Mesoporous Silica Nanoparticles Enhances the Efficacy of Chemotherapy in Multidrug-Resistant Cancer Cells. *Small* **2009**, *5*, 2673–2677.
34. Hong, X.; Yang, Z. Y.; Wang, M.; Lu, L.; Li, Y. H.; Hao, X. S.; Chen, G. Y. Multidrug Resistance-Associated Protein 3 and Bcl-2 Contribute to Multidrug Resistance by Vinorelbine in Lung Adenocarcinoma. *Int. J. Mol. Med.* **2011**, *28*, 953–960.
35. Lage, H. An Overview of Cancer Multidrug Resistance: A Still Unsolved Problem. *Cell. Mol. Life Sci.* **2008**, *65*, 3145–3167.
36. Wu, L. L.; Zou, Y.; Deng, C.; Cheng, R.; Meng, F. H.; Zhong, Z. Y. Intracellular Release of Doxorubicin from Core-Crosslinked Polypeptide Micelles Triggered by Both pH and Reduction Conditions. *Biomaterials* **2013**, *34*, 5262–5272.

37. Meng, F. H.; Zhong, Y. A.; Cheng, R.; Deng, C.; Zhong, Z. Y. pH-Sensitive Polymeric Nanoparticles for Tumor-Targeting Doxorubicin Delivery: Concept and Recent Advances. *Nanomedicine* **2014**, *9*, 487–499.
38. Son, S.; Nam, J.; Kim, J.; Kim, S.; Kim, W. J. i-Motif-Driven Au Nanomachines in Programmed siRNA Delivery for Gene-Silencing and Photothermal Ablation. *ACS Nano* **2014**, *8*, 5574–5584.
39. Gueron, M.; Leroy, J. L. The i-motif in Nucleic Acids. *Curr. Opin. Struct. Biol.* **2000**, *10*, 326–331.
40. Sharma, J.; Chhabra, R.; Yan, H.; Liu, Y. pH-Driven Conformational Switch of "i-motif" DNA for the Reversible Assembly of Gold Nanoparticles. *Chem. Commun.* **2007**, 477–479.
41. Jones, M. R.; Macfarlane, R. J.; Lee, B.; Zhang, J. A.; Young, K. L.; Senesi, A. J.; Mirkin, C. A. DNA-Nanoparticle Superlattices Formed from Anisotropic Building Blocks. *Nat. Mater.* **2010**, *9*, 913–917.
42. Liu, J.; Lu, Y. Preparation of Aptamer-Linked Gold Nanoparticle Purple Aggregates for Colorimetric Sensing of Analytes. *Nat. Protoc.* **2006**, *1*, 246–252.
43. Macfarlane, R. J.; Jones, M. R.; Senesi, A. J.; Young, K. L.; Lee, B.; Wu, J. S.; Mirkin, C. A. Establishing the Design Rules for DNA-Mediated Colloidal Crystallization. *Angew. Chem., Int. Ed.* **2010**, *49*, 4589–4592.
44. Choi, C. H.; Hao, L.; Narayan, S. P.; Auyeung, E.; Mirkin, C. A. Mechanism for the Endocytosis of Spherical Nucleic Acid Nanoparticle Conjugates. *Proc. Natl. Acad. Sci. U.S.A.* **2013**, *110*, 7625–7630.
45. Jensen, S. A.; Day, E. S.; Ko, C. H.; Hurley, L. A.; Luciano, J. P.; Kouri, F. M.; Merkel, T. J.; Luthi, A. J.; Patel, P. C.; Cutler, J. I.; *et al.* Spherical Nucleic Acid Nanoparticle Conjugates as an RNAi-Based Therapy for Glioblastoma. *Sci. Transl. Med.* **2013**, *5*, 209.
46. Zheng, D.; Giljohann, D. A.; Chen, D. L.; Massich, M. D.; Wang, X. Q.; Iordanov, H.; Mirkin, C. A.; Paller, A. S. Topical Delivery of siRNA-Based Spherical Nucleic Acid Nanoparticle Conjugates for Gene Regulation. *Proc. Natl. Acad. Sci. U.S.A.* **2012**, *109*, 11975–11980.